Nanoscopic time crystal obtained by nonergodic spin dynamics

Carla Lupo and Cedric Weber
Theory and Simulation of Condensed Matter, King's College London, The Strand, London WC2R 2LS, United Kingdom

(Received 24 July 2018; published 25 November 2019)

We study the far-from-equilibrium properties of nanoscopic classical spin systems. In particular, we focus on the interplay between lattice vibrations and magnetic frustrations induced by surface effects in antiferromagnets. We use an extended Monte Carlo simulations which treats both the ionic degrees of freedom and spin variables on the same footing via a Heisenberg-Lennard-Jones Hamiltonian with a spin-lattice coupling. The interplay of the local ordered magnetic moments and the lattice dynamics provides, at zero temperature, a structural phase diagram characterizing the magnetic order in two different antiferromagnetic nanoclusters. At nonzero temperature, the competition between spins and the ionic vibrations considerably affects the magnetization of these systems. Next, we explore the dynamical response of the antiferromagnetic structures subjected to an initial ferromagnetic quench by solving the stochastic Landau-Lifshitz-Gilbert equation at finite temperature. The dynamics reveals a nontrivial structure-induced behavior in the spin relaxation with a concomitant memory of the initially applied ferromagnetic quench. These observations of long-lived nonthermal states could open new avenues in nanotechnology.

DOI: 10.1103/PhysRevB.100.195431

I. INTRODUCTION

Many-body systems comprise a wide range of systems, from simple metals and organic molecules all the way up to cells. While their physics can be extremely rich, this complexity is, however, often irrelevant, as such systems will typically—at equilibrium—thermalize, a process through which most information about their preparation history and their initial state is lost [1,2]. This behavior is typical for ergodic systems in the thermodynamic limit and allows us to calculate physical observables and make predictions that can be measured and tested. However, ergodicity can be broken out of equilibrium [3], in particular by inducing nonthermal states that keep a memory of their initial condition for long times. Those peculiar behaviors have been explored in novel nonequilibrium phases of matter, which includes Floquet symmetry-protected topological phases [4,5] and time crystals [6–11]. In particular, out-of-equilibrium quantum materials have been extensively studied theoretically, with a range of quantum approaches, such as the Floquet dynamical mean-field theory [12] used for electron-spin systems [13,14] and nonequilibrium Green's function techniques for electron-phonon dynamics [15,16]. While bulk systems have been extensively investigated, nanoscopic systems remain open to questions. Recent progress in nanoengineering, such as the design of single-atom arrays as memory devices [17], has opened new possibilities to explore quantum states in systems where thermalization is not obtained, in particular for quenched and periodically driven systems. Indeed, it has been observed that finite-size effects allow these systems to keep a much better local memory of their initial conditions [18]. Experimental advances in manipulation and switching of the magnetization—possible even at the femtosecond level [19]—have triggered new studies in spin dynamics [20] towards the microscopic understanding of emerging relaxation timescales and the discovery of new suitable candidates for magnetic-logic building blocks [20]. Particular attention has been paid when antiferromagnetic order is involved [21,22]: in these systems the contribution of the uncompensated spins at the surface triggers exotic phenomena which are not analytically tractable and whose precise understanding is still unknown. To that end, new mechanisms for slow relaxation and nonergodicity have potential implications for the design and control of novel quantum nonequilibrium materials and devices. Atomistic electron-spin models have proved to be a powerful approach to model ultrafast magnetization dynamics.

In this work, we propose a study of the dynamics of a typical many-body nanoscopic system in which the relaxation processes involve both the structure and magnetic moments. We consider the quenched and driven classical spins in the presence of long-range magnetic interactions coupled to the lattice dynamics. We first focus on the interplay of the local ordered magnetic moments and the lattice dynamics at finite temperature. Next, we extend the equilibrium calculations to a ferromagnetic quench. We go on to study the equilibrium and out-of-equilibrium properties using a combination of Monte Carlo simulations [23,24] and atomistic spin dynamics [25,26] through the numerical implementation of the Landau-Lifshitz-Gilbert [27] equation extended to deal with finite temperatures within a Langevin dynamics framework.

II. EQUILIBRIUM PROPERTIES OF MAGNETIC NANOCLUSTERS

We consider a cluster in a spherical shape and a simple cubic structure with a unitary lattice constant. The total

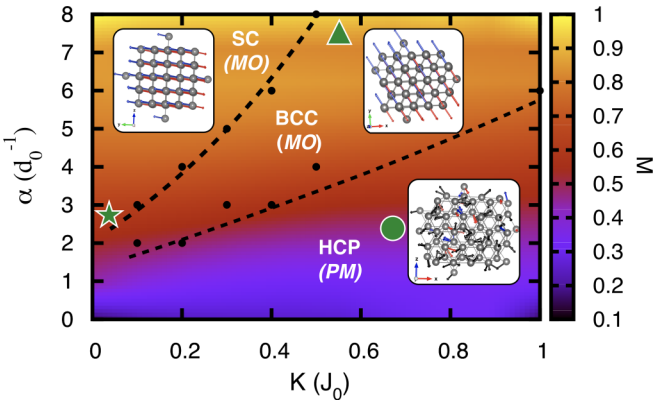

FIG. 1. Zero-temperature structural phase diagrams with respect to the interaction range α and the Lennard-Jones potential K. Dashed lines are guides to the eyes and distinguish three different structural regions: simple-cubic (sc, e.g., ⋆, $LaTiO_3$), bcc (e.g., △, MnO) and hcp (e.g., ◯, Ni). Shaded colors indicate the presence of antiferromagnetic order (MO). The arrows represent one possible spin configuration for the collinear magnetic order [at $\mathbf{Q} = (\pi, \pi, \pi)/a$ for SC and $\mathbf{Q} = (0, 0, 2\pi)/a$ for bcc] and magnetic disorder for hcp. The system in the analysis has 123 sites.

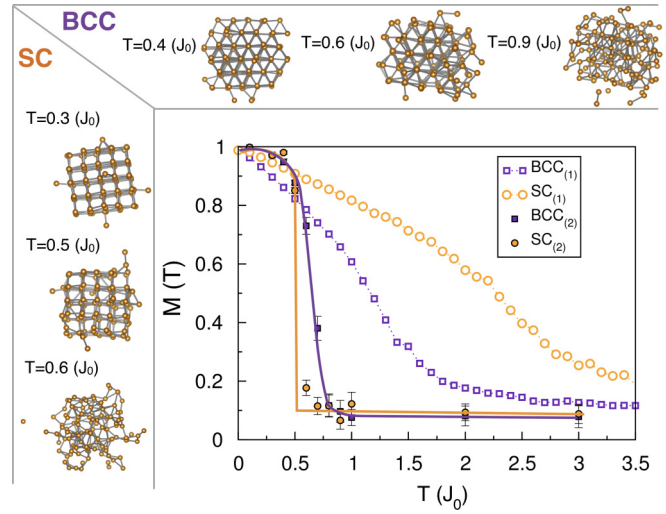

FIG. 2. Temperature-dependent behavior of the magnetic order parameter obtained running equilibrium simulations with ($sim_{(2)}$) and without ($sim_{(1)}$) considering the coupling of the spins with the lattice deformation. The two structures considered are SC (orange) and bcc (violet). The top and left panels show the structures obtained at finite temperature.

lattice-spin Hamiltonian of the cluster reads as follows:

$$H = -\sum_{i,j} J(d_{ij})\mathbf{S}_i \cdot \mathbf{S}_j + K \sum_{i,j} \left[\left(\frac{d^0}{d_{ij}}\right)^{12} - 2\left(\frac{d^0}{d_{ij}}\right)^{6} \right], \tag{1}$$

where $\mathbf{S}_i$ are $O(3)$ unitary $|\mathbf{S}| = 1$ spins ruled by a Heisenberg Hamiltonian with an inhomogeneous superexchange coupling $J(d_{ij}) = J_0\, e^{-\alpha d_{ij}}$, where J_0 is the antiferromagnetic nearest-neighbor interaction. The exchange interaction function $J(d_{ij})$ can be tuned from *ab initio* calculation or experimental results [25,28].

The α parameter scales the range of the interaction: as α decreases, the interaction becomes long range. The lattice deformation is constrained by a Lennard-Jones (LJ) potential with a normalized unit distance ($d_0 = 1$). We use extended Monte Carlo Metropolis calculations with both spins and an ionic displacement update [28–31].

The competition between the Heisenberg term and the Lennard-Jones potential, respectively tuned by the α and K parameters introduced in Eq. (1), stabilizes three different ground-state structures (Fig. 1): simple cubic (sc), bcc, and hcp. These structures are obtained if the system optimizes either the superexchange potential or the ionic interactions (LJ). When the dominant contribution to the energy is the exchange term, the structure is SC, with a concomitant lattice compression. Indeed, the SC structure accommodates the largest number of nonfrustrated antiferromagnetic bonds in three dimensions. For larger K, we obtain a competition between the exchange and LJ terms. This drives a structural transition towards a bcc structure, which increases the coordination number, albeit retaining an ordered spin structure with a pitch vector [$\mathbf{q} = (0, 0, 2\pi/a)$]. These two cases show magnetic order (MO). For $K \gg 1$ the leading contribution comes from the LJ potential, and the system increases its coordination number further, losing the magnetic order in favor of the more compact hcp structure. Under the assumption of large magnetic moment, paradigmatic systems for the model above are represented by antiferromagnetic sc structures such as perovskites (e.g., $LaTiO_3$ [32–34]), bcc nanoclusters such as Mn [35–37], and the hcp Ni nanoparticle [26,38,39]. (Symbols in Fig. 1 identify the different materials with parameters listed in Table I).

To summarize, we note that the spin-exchange and Lennard-Jones terms compete in a nontrivial fashion in the presence of antiferromagnetic interaction: on the one hand, the Lennard-Jones term favors the most compact structure, e.g., the hcp, although this phase is magnetically frustrated, and on the other hand, the optimal phase to accommodate antiferromagnetism in three dimensions is the regular cubic lattice. This leads to a very rich phase diagram at zero temperature, as mentioned above, but also induces nontrivial effects at finite temperature (Fig. 2). We now turn to finite-temperature calculations of the structures with zero-temperature magnetic order (sc and bcc in Fig. 1). In the absence of the ionic motion, the magnetic order parameter of the sc phase $sc_{(1)}$ is stable until $T \approx 3[J_0]$, whereas for the frustrated bcc phase $bcc_{(1)}$ we find a less stable magnetic phase (magnetic for $T < 1.8[J_0]$). However, once both the spin and ionic potential are considered ($sc_{(2)}$, $bcc_{(2)}$), we observed that both structures are magnetic for $T < 0.6[J_0]$, but the processes leading to the paramagnetic phase are very different. For the sc phase, we observe that the drop in magnetization is concomitant with a loss of the structural properties, as the lattice starts melting at $T \approx 0.6[J_0]$ (as shown in the left panel), whereas the bcc structure survives above this temperature (as shown in the top panel) and undergoes a magnetic transition towards the paramagnetic phase due to magnetic fluctuations. The nonzero magnetization value at high temperature is due to the finite size of the system. We observe that the values of M of $sc_{(1)}$ and

bcc$_{(1)}$ at $T = 5[J_0]$ are different due to different contributions of the surface spins.

III. DYNAMICAL RESPONSE TO EXTERNAL FIELDS AND MEMORY EFFECTS

We now turn to the discussion of the time evolution after a ferromagnetic quench. We focus here on the time evolution of the system at low enough temperature (far from the melting temperature), where the structure is weakly dependent on temperature and can be considered fixed. We calculate the dynamical magnetic properties of the nanostructure far from equilibrium, with the Landau-Lifshitz-Gilbert formalism, which accounts for only the time evolution of the spin degrees of freedom, and the structural properties are obtained for the sc and bcc magnetic systems shown in Fig. 1. The Landau-Lifshitz-Gilbert equation has been numerically solved by replacing the spin operators of the Heisenberg Hamiltonian with classical angular momentum vectors. The evolution of each spin can be seen as its precession around an effective field $\mathbf{\Omega}_i = -\sum_{j\neq i} J_{ij}\mathbf{S}_j$ induced by the neighboring spins. Furthermore, to induce energy dissipation, the system is physically embedded in a thermal bath at constant temperature, mathematically represented by a stochastic field and a dissipative term in the equation. The differential equation of motion reads

$$\frac{d\mathbf{S}_i}{dt} = \frac{1}{\hbar}\{\mathbf{S}_i \times (-\mathbf{\Omega}_i + \mathbf{h}_i) - \gamma \mathbf{S}_i \times [\mathbf{S}_i \times (-\mathbf{\Omega}_i)]\}, \quad (2)$$

where $\mathbf{h}_i$ is a Gaussian-distributed white noise with zero mean and vanishing correlator $\langle h_i(t)h_j(t')\rangle = \mu\delta_{i,j}\delta(t,t')$, representing the stochastic field. Its value at each time step Δt is $h_{\alpha,i} = \eta\sqrt{\mu/\Delta t}$, with $\alpha \in \{x, y, z\}$ being the Cartesian coordinate and i referring to the site label; $\eta \sim \mathcal{N}(0, 1)$ is a random variable sampled from the standard normal distribution. γ is the Gilbert dissipation parameter related to the stochastic field through the fluctuation-dissipation theorem (FDT) [40,41] $\mu = 2\gamma k_B T$ at equilibrium. We point out that γ is a dimensionless parameter that can be extracted directly from the spin dynamics simulation or by comparison with Monte Carlo calculations at equilibrium. We found that both are consistent within the error bars (Fig. 7). The dynamics is implemented via the Suzuki-Trotter decomposition outlined in Refs. [42,43], and time units have been fixed assuming the exchange interaction is of the typical order of magnitude of the bulk $J = 0.1$ eV.

Spin dynamics after a ferromagnetic quench. Since we are interested in the response of the system to an initial out-of-equilibrium condition, we start from the ferromagnetic configuration and let the system evolve. At low temperature ($T = 0.001[J_0]$, Fig. 3(a)) the central site of the nanostructures (blue line for sc and red for bcc) antialigns with respect to its initial configuration along the z direction under the effect of the evolution operator. The response of the lattice to this mechanism is prompt: the flipping mechanism diffuses from the core spin to the surface ones (Fig. 8), and the evolution of all spins is synchronized toward the relaxation to the antiferromagnetic (AF) state by keeping a global orientation on each of the sublattices. Red and blue lines in Figs. 3(a) and 3(b) represent the evolution of the z component of two spins belonging to ferromagnetic sublattices A and B. The

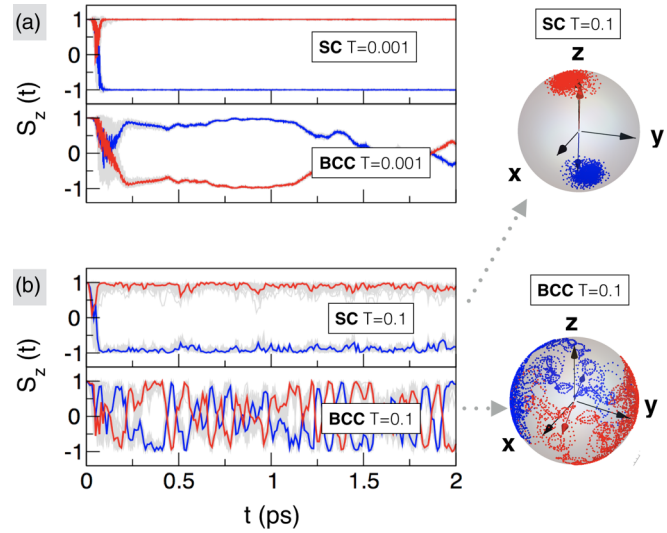

FIG. 3. (a) and (b) Time evolution of the z component $S_z(t)$ of all the spins (gray solid lines) in the system initially subjected to a ferromagnetic quench: blue and red solid lines refer to two sites with opposite magnetic moments after the transient. Results are shown for $T = 0.001, 0.1[J_0]$, respectively, for sc and bcc. On the side, the spin configuration at $T = 0.1[J_0]$ for two different sites (blue and red) with opposite magnetic moments at the steady state is shown.

dynamics of the local vector on each site is also shown via the gray shaded area, and it shows that the time dynamics is synchronous. We note, however, that, different from the bcc, at $T = 0.001[J_0]$ [Fig. 3(a)] in the sc only one sublattice is evolving under the time evolution operator, while the other is not affected by the dynamics, and the orientation of the initially applied ferromagnetic field $\mathbf{B}_Q = (0, 0, 1)$ is retained (red line). This nontrivial dynamics is triggered by the exchange coupling between the sublattices in the AF phase when the system is initially prepared out of equilibrium. The spontaneous locked polarization of the magnetization in the sc is due to its intrinsic weak ferromagnetic component. Indeed, even if both sc and bcc are able to stabilize a Néel order along all the directions, they differ in the number of uncompensated spins (10% sc and 0.1% bcc). Thus, while for bcc the flipping mechanism happens at ≈2 ps, for the sc it occurs at $t \approx 0.4$ ns for fixed $T = 0.001[J_0]$ [see Fig. 10(a)]. We now consider the dynamics at higher temperatures $T = 0.1[J_0]$ [Fig. 3(b)] where the systems are still magnetic. We observe that while for the bcc ergodicity is recovered, for sc the obtained time evolution is similar to the $T = 0.001[J_0]$ case with thermally activated small oscillations around the initial quenching field $\mathbf{B_Q}$. The results discussed so far for a short time window, $t_f = 2$ ps, are extended up to $t_f = 12$ ps. In Fig. 4 we considered the histogram $P(S_z)$ of the z-axis spin component obtained along the time-dependent trajectories at different temperatures T. Note that for an ergodic system, the histogram is uniform, as obtained for $T > 0.1[J_0]$. For $T < 0.1[J0]$, the spins evolve along a constrained time trajectory, with a nonuniform distribution of the spin components, which is a signature of a nonthermal state. We hence observe in the sc long-lived nonthermal states, which are nontrivial topologically protected states driven by the interplay of the

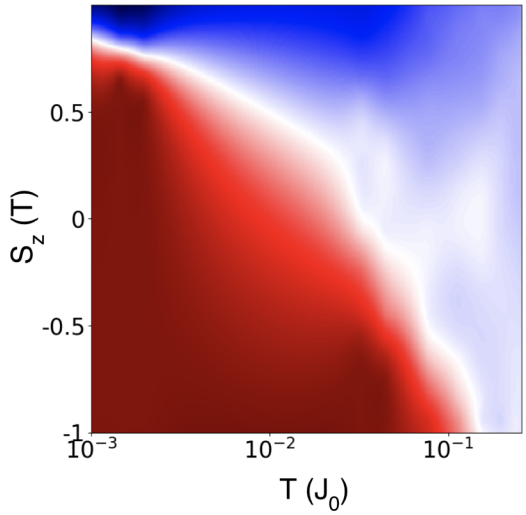

FIG. 4. Histogram $P(S_z)$ of the z-axis spin component obtained along the time-dependent trajectories at different temperatures T in the sc. The color map goes from 0 (red) to 1 (blue). Dynamics considered up to $t_f = 12$ ps.

initial quench and long-range interactions. On the other hand, in the bcc, whose structure is not bipartite, the intrinsic magnetic anisotropy due to the geometry does not stabilize a long-lived memory effect against thermal fluctuation.

Adding a static field. Interestingly, time translational symmetry observed in the transient in Fig. 3(a) is explicitly broken when an applied magnetic field $\mathbf{h} \to \tilde{\mathbf{h}} = \mathbf{h} + \mathbf{h}_{\rm ext}$ with $h_{{\rm ext},i=\{x,y,z\}} = h_{\rm ext}$ is switched on [Eq. (2)] after the ferromagnetic quench $\mathbf{B_Q}$. Indeed, the spin dynamics after the quench and an applied field shows a periodic behavior. Here we consider a small external field ($h_{\rm ext} = 0.01, 0.1$), and we observe the dynamics in the temperature regime where the effects of the small field are not washed away by thermal fluctuations. Figure 5(a) shows that while for the bcc cluster the staggered magnetic vector stabilizes along the direction of the field, in the sc cluster the dynamics is characterized by long-lived oscillations and the alignment is recovered at $t = 20$ ps for $T = 0.001[J_0]$, $h_{\rm ext} = 0.1$ [Fig. 10(b)]. Thus, in the sc the dynamics after the quench is characterized by two timescales. First, at a femtosecond scale the antiferromagnetic interaction brings the system toward its energy minimum: the spins after the ferromagnetic quench follow the same relaxation as in the absence of applied field at first and form an AF state. Second, at a larger timescale the AF state symmetry is maintained, and the spins precess around the $\mathbf{h}_{\rm ext}$ direction: this nontrivial dynamics which brings the system towards the alignment along the direction of the external field is characterized by an observable timescale [Fig. 10(b)]. The arising of this intermediate phase between the AF stabilization and the alignment with the external field, characterized by a periodic response of the system to a static field, is exclusively triggered by the uncompensated spins in the AF nanocluster. The scenario at $T = 0.01$ and $h_{\rm ext} = 0.01$ [Fig. 5(b)] shows that the periodic phase persists even for higher temperature and smaller field: indeed, while in the bcc the thermal fluctuations destroyed the effect of $\mathbf{h}_{\rm ext}$, in the sc the periodic oscillations are still evident.

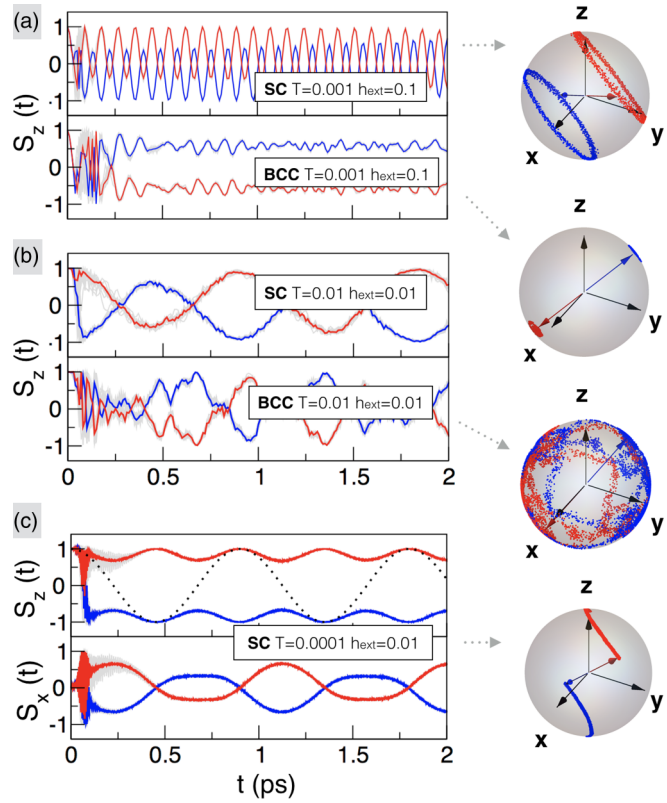

FIG. 5. (a) and (b) Time evolution of the z component $S_z(t)$ of all the spins (gray solid lines) in the system initially subjected to a ferromagnetic quench at $t = 0$ and a static field for $t > 0$. Blue and red solid lines refer to two sites with opposite magnetic moments after the transient. Results are shown for different temperatures and values of the fields $h_{\rm ext}$ for sc and bcc. (c) Time evolution of the x and z components of the spins $S(t)$ in the system subjected to a ferromagnetic quench at $t = 0$ and an AC field (black dashed lines $\mathbf{h_{AC}}/h_{\rm ext}$) for $t > 0$. On the side, the spin configurations for two different sites are shown.

Thus, we discover an interesting phase of the transient triggered by the AF interactions in a finite system where the response to a static field shows a periodic behavior with an observable and tunable relaxation timescale.

Adding an AC field. Finally, we study the response of the sc system to an AC field $\mathbf{h} \to \tilde{\mathbf{h}} = \mathbf{h} + \mathbf{h}_{\rm ext} \cos(2\pi\omega t)$ after the ferromagnetic quench $\mathbf{B_Q}$. Figure 5(c) shows the dynamics of the spins in the time crystal phase. In the latter phase, the time evolution is not periodic with the applied field, and in particular we find that the component of the spin aligned in the quenched direction (e.g., along the z axis) oscillates with a frequency which is double the applied field (see Fig. 6). In our setup, we typically use an applied field in the terahertz range (1.1 THz). Note that further subharmonics are also present with albeit smaller amplitudes. Thus, the initial ferromagnetic quench and the oscillating applied field prevent the spins from completing a full precession, and instead, the covered phase space is limited to a portion of the AF precession circles. The spin trajectories explicitly break the time invariance observed in Fig. 3(a) and enter into a periodic motion that lasts beyond the largest time considered in our calculations [≈1 ns, Fig. 10(d)].

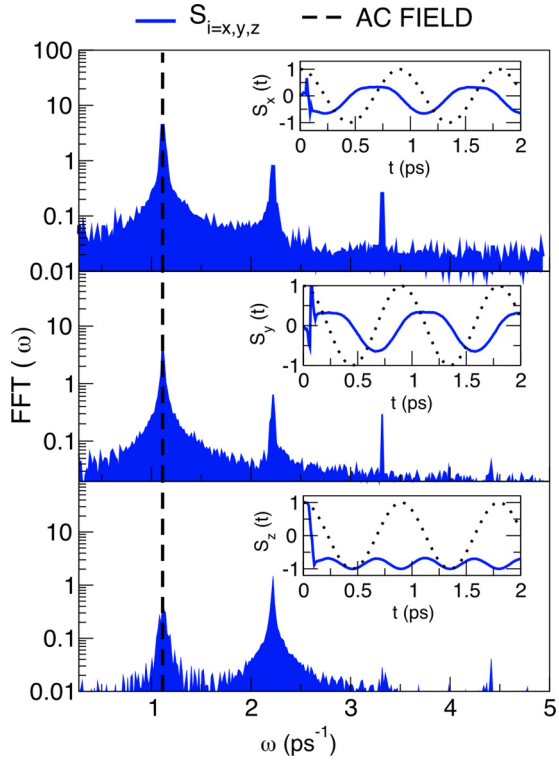

FIG. 6. Fourier analysis of the core spin trajectories (blue solid lines) compared with the AC field $\mathbf{h}_{\mathbf{AC}} = \mathbf{h}_{\mathrm{ext}} \cos(2\pi\omega t)$ (black dashed lines for $\mathbf{h}_{\mathbf{AC}}/h_{\mathrm{ext}}$). Results are shown for fixed $T = 0.0001$ and $h_{\mathrm{ext}} = 0.01$ values. Time window considered after the transient up to 70 ps.

This nontrivial time translational symmetry breaking, which protects the $\mathbb{Z}_2$ topology of the spin trajectories for macroscopic timescales, bears similarities to the time crystal [9] recently observed experimentally in magnetic systems [10]. In our calculations, the time crystal phase (TC) stems from nonthermal states triggered by the nontrivial dynamics obtained after the quench, when, at $T = 0.0001[J_0]$, only one of the bipartite sublattices evolves with time, whereas the other sublattice stays aligned with the applied magnetic field $\mathbf{B_Q}$ and remains topologically protected upon application of AC field. At finite but small temperatures this dynamics breaks the time translational invariance and the spherical symmetry of the spins and in turn provides a nanoscopic time crystal with the magnetic vector aligned along a preferred orientation (induced by a combination of the initial quench and applied magnetic field). Thus, in the TC phase we observe nonthermal states and violation of the FDT (Fig. 9). The loss of the time crystal is, in particular, accelerated by an increase of the dissipation term γ [Eq. (2); see Fig. 11(a)] or the temperature [Fig. 11(b)], as thermalization happens on faster timescales.

IV. CONCLUSIONS

In conclusion we provided the results of the role of the spin-lattice coupling in the equilibration of an antiferromagnetic nanoscopic system at both zero and finite temperature. We then focused on the spin quenched dynamics in a temperature regime which foregoes the melting of the magnetic moment. We demonstrated slow relaxation and nonergodicity in nondisordered nanoscopic many-body systems induced by the initial magnetic quench. The nonthermal states persist in the presence of experimentally controllable classical thermal noise, and the signatures of metastability are uncovered in situations where nonergodicity is transient only due to dissipation. Our work lays out foundations for future experiments in small antiferromagnetic nanoparticles [32,44,45]. Furthermore, it provides numerical results for future realization of antiferromagnetic memory devices in which magnetocrystalline anisotropy [18] and tunability of the exchange coupling [46] play a crucial role.

ACKNOWLEDGMENTS

We gratefully acknowledge insightful discussions with S.L. Dudarev and P.-W. Ma. C.L. is supported by the EPSRC Centre for Doctoral Training in Cross-Disciplinary Approaches to Non-Equilibrium Systems (CANES, Grant No. EP/L015854/1). C.W. is funded by the EPSRC Grant No. EP/R02992X/1. This work has been performed using resources provided by the Cambridge Tier-2 system operated by the University of Cambridge Research Computing Service (https://www.hpc.cam.ac.uk) funded by EPSRC Tier-2 capital Grant No. EP/P020259/1. C.W. gratefully acknowledges the UK Materials and Molecular Modelling Hub for computational resources, which is partially funded by EPSRC (Grant No. EP/P020194/1). We are grateful for computational support from the UK national high performance computing service, ARCHER, for which access was obtained via the UKCP consortium and funded by EPSRC Grant Ref EP/P022561/1.

APPENDIX A: MONTE CARLO SIMULATION

As reported in the main text, at zero temperature the competition between the Heisenberg term and the Lennard-Jones potential, respectively tuned by the α and K parameters introduced in Eq. (1), stabilizes three different ground-state structures (Fig. 1): simple cubic (sc), bcc, and hcp. These structures are obtained if the system optimizes either the superexchange potential or the ionic interactions (LJ). Under the assumption of large magnetic moment, paradigmatic systems for the model above are represented by antiferromagnetic sc structures such as perovskites (e.g., $LaTiO_3$ [32–34]), bcc nanoclusters such as Mn [35], and the hcp Ni nanoparticle [26,38,39]. An estimation of the order of magnitude of the parameters (α, K) for the examples provided above can be inferred by combining two features: (i) the structural properties, e.g., bond lengths, coordination number, and the radial distribution function, of the clusters obtained in our simulation and (ii) the model of the exchange interaction and Lennard-Jones potentials used, respectively, for the bulk and nanoclusters available in the literature.

A sensible estimation of the α parameter is obtained from the analysis of the exchange interaction for a selected element or compound. In particular we will use the Bethe-Slater equation properly parametrized for a given element or material (e.g., in Refs. [26,37]) or the computed nearest (J_1) and the next-nearest (J_2) exchange coupling obtained mapping

TABLE I. (K, α) parameters inferred for the three paradigmatic systems provided as examples for the magnetostructural phases in Fig. 1.

	K (eV)	α (Å^{-1})
Ni	0.66 [39]	2.18 [26]
Mn	0.55 [36]	7.84 [37]
$LaTiO_3$	0.02 [33]	2.79 [34]

the density functional theory (DFT) energies to a classical Heisenberg model [34]. α is obtained in units of Å^{-1}. The LJ interaction is extracted from previous works and molecular dynamics calculations carried out in Refs. [33,36,39]. K is obtained in units of eV.

We report in Table I the inferred values of (K, α) for the clusters under analysis, properly supported by several references. We emphasize, however, that such a correspondence between values obtained by *ab initio* DFT and the Heisenberg theory remains at the qualitative level, as quantum fluctuations are not included for classical spin systems.

APPENDIX B: SPIN DYNAMICS SIMULATION

1. Benchmark of stochastic time-dependent calculations against Monte Carlo simulations

Insights on the dynamical magnetic properties of the nanostructures stabilized so far at equilibrium are obtained by running spin dynamics simulations. The Landau-Lifshitz-Gilbert equation in Eq. (2) was numerically solved by replacing the spin operators of the Heisenberg Hamiltonian with classical angular momentum vectors. γ is the Gilbert dissipation parameter related to the stochastic field through the fluctuation dissipation theorem (FDT) [40,41] $\mu = 2\gamma k_B T$ at equilibrium. We point out that γ is a dimensionless parameter that can be extracted directly from the spin dynamics simulation or by comparison with Monte Carlo calculations at equilibrium. In Fig. 7, we show the magnetic order parameter obtained with *heat bath* simulations and the spin dynamics. Thus, the temperature obtained under the hypothesis that FDT is satisfied during the dynamics of the spins [42] can also be obtained by the equilibrium Monte Carlo simulation.

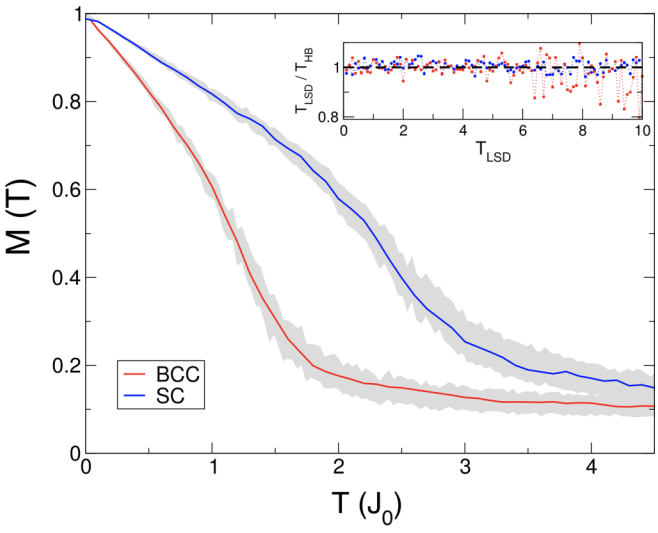

FIG. 7. Magnetic order parameter as a function of temperature obtained for two different systems (sc in blue and bcc in red). The gray shaded regions represent the Langevin statistics. The inset shows the match between the temperature obtained with the *Langevin spin dynamics* (T_{LSD}) and the Monte Carlo *heat bath* (T_{HB}) results.

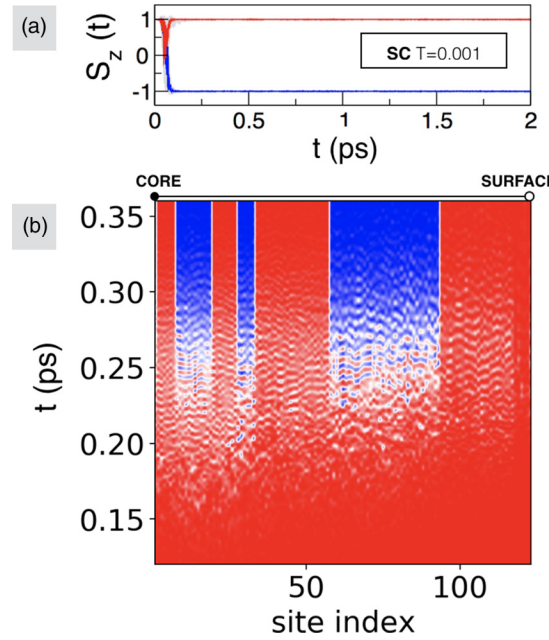

FIG. 8. (a) Time evolution of the z component $S_z(t)$ of all the spins (gray solid lines) in the system initially subjected to a ferromagnetic quench: blue and red solid lines refer to two sites with opposite magnetic moments after the transient. Results are shown for $T = 0.001[J_0]$ for the sc nanocluster. (b) Details of the flipping mechanism during the transient at $T = 0.001[J_0]$, which starts from the core site toward the surface. Sites are labeled according to their distance from the center.

2. Insights on the spin dynamics results

(a) Spin dynamics after a ferromagnetic quench: bcc versus sc nanoclusters. We now turn the discussion to the response of the system to an initial out-of-equilibrium condition. Thus, we initialize the system in the ferromagnetic configuration along the z axis, and we let the system evolve with the exponential time evolution operator for the spins given by Eq. (1). As we discussed in the main text, at low temperature ($T = 0.001[J_0]$, Fig. 8(a)) the central site of the nanostructures (blue solid line) antialigns with respect to its initial configuration along the z direction under the effect of the evolution operator. The time dependence of the local vector on each site is also shown in Fig. 8(b), where the sites are labeled according to their distance from the center and the color map refers to the value of the z component for each spin $S_z(t)$ from $+1$ (red) to -1 (blue). We note that the flipping mechanism during the transient at $T = 0.001[J_0]$ starts from the central site toward the surface and the evolution of all spins is synchronized toward the relaxation to the AF state by keeping a global orientation on each of the sublattices. As we observed already

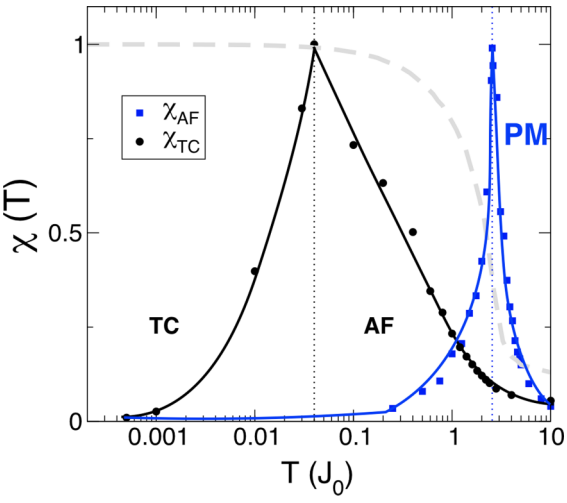

FIG. 9. Temperature-dependent behavior of the fluctuations of the order parameter both along the time evolution after the quench (black circles) and at the equilibrium one (blue squares). The plot highlights the arising of three different regions: the time crystal (TC), the magnetically ordered phase (antiferromagnetic AF), and the paramagnetic phase (PM). The structure under analysis is the sc. The gray dashed line is the staggered magnetic order parameter squared.

in the main text, the sc nanostructure shows a locked direction of the spin along the z axis up to $t \approx 0.4$ ns for fixed $T = 0.001[J_0]$ [see Fig. 10(a) below].

To complete the understanding of this phase with spontaneous locked polarization of the magnetization in the sc cluster, we considered in Fig. 4 the histogram $P(S_z)$ of the z-axis spin component obtained along the time-dependent trajectories for a calculation extended up to $t_f = 12$ ps. Note that for an ergodic system, the histogram is uniform, as obtained for $T > 0.1J_0$. For $T < 0.1J_0$, the spins are evolving along a constrained time trajectory, with a nonuniform distribution of the spin components, which is a signature of a nonthermal state.

We now want to look at the average quantities which characterize the dynamics of the structures considered, and we use the FDT to search for evidence of the nonthermal states observed above. In the following analysis we focus on the sc for which, due to its bipartite structure, the memory effect is enhanced and resistant against thermal fluctuation even in the absence of magnetic anisotropy. In Fig. 9 we calculate both the correlation of the order parameter along the time evolution after the quench and its fluctuations at equilibrium as $\chi_{\mathbf{q}=\mathrm{AF}}(T)$ [where the wave-vector-dependent magnetization $M_{\mathbf{q}} = (1/N)\sum_i \mathbf{S}_i e^{i\mathbf{q}\cdot\mathbf{r}_i}$ has $\mathbf{q}$ corresponding to an ordering wave vector defined for the bulk antiferromagnetic states $\mathbf{q} = (\pi, \pi, \pi)/a$ for sc]. At equilibrium, the two quantities are related by the FDT. However out of equilibrium, in the case of a nonergodic dynamics, a violation of the FDT theorem can be observed for a nonthermal state. We observe indeed in our calculations the presence of long-lived nonthermal states obtained after the quench, violating the FDT, at temperature $T < 0.01[J_0]$ for sc (and $T < 0.0001[J_0]$ for bcc). We hence found three different phases: (i) nonergodic but magnetic (TC), (ii) ergodic and magnetic (AF), and (iii) paramagnetic (PM). In particular, the first phase is named a time crystal phase because of time translational invariance.

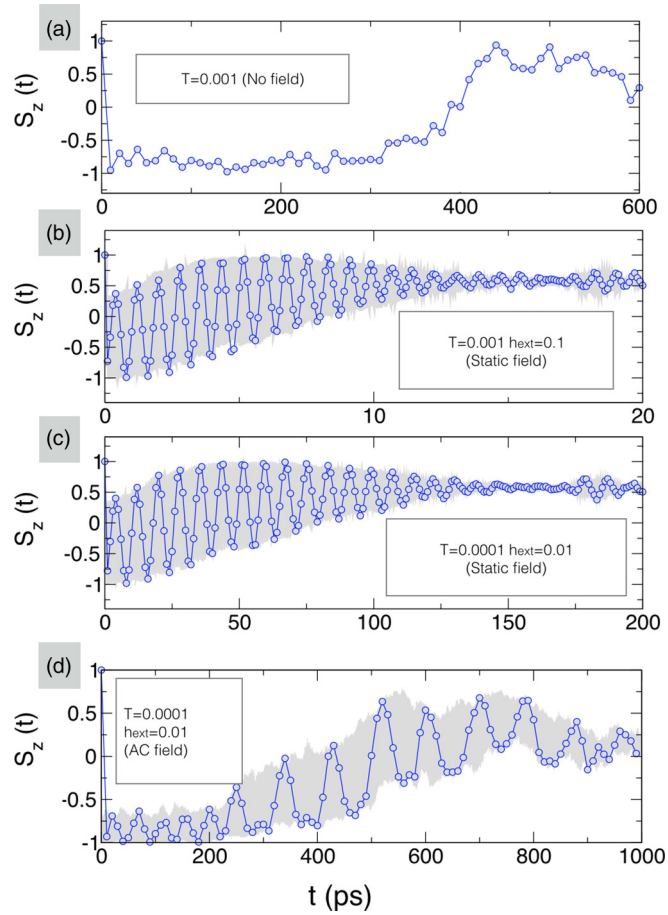

FIG. 10. (a) Time evolution of the z component $S_z(t)$ of the core spin (blue line with dots) in the antiferromagnetic sc subjected to three different protocols. System initially ($t = 0$) subjected to a ferromagnetic quench and subsequently let to evolve in the absence of any external drive [long-time dynamics of Fig. 3(a) in the main text]. (b) and (c) Ferromagnetic quench ($t = 0$) and a static field $\mathbf{h_S} = \mathbf{h}_{\mathrm{ext}}$ at $t > 0$ [long-time dynamics of Fig. 5(a) in the main text]. (d) Ferromagnetic quench ($t = 0$) and an AC field $\mathbf{h_{AC}} = \mathbf{h}_{\mathrm{ext}} \cos(2\pi\omega t)$ [long-time dynamics of Fig 5(c) in the main text]. Results are shown for different temperatures and h_{ext} values.

(b) Long-time dynamics under the effect of different driving fields. The results discussed so far for a short time window ($t_f = 2$ ps) are extended up to $t_f = 1$ ns in Fig. 10, where we consider the time evolution of the z component $S_z(t)$ of the core spin (blue line with dots) in the antiferromagnetic sc subjected to a ferromagnetic quench at $t = 0$ and three different protocols at $t > 0$: (i) the absence of any external drive in Fig. 10(a), (ii) the introduction of an isotropic static field $\mathbf{h_S} = \mathbf{h}_{\mathrm{ext}}$ at $t > 0$ in Figs. 10(b) and 10(c), and (iii) an AC field $\mathbf{h_{AC}} = \mathbf{h}_{\mathrm{ext}} \cos(2\pi\omega t)$ in Fig. 10(d). In our results we considered small external fields ($h_{\mathrm{ext}} = 0.1, 0.01$), and we observe the dynamics in the temperature regime where the effects of the small field are not washed away by thermal fluctuations. As we discussed before, the locked dynamics

shown in Fig. 3(a) after the ferromagnetic quench lasts up to 400 ps, as shown in Fig. 10(a). We now want to look at the effect of introducing a driving field to this long-lived nonthermal state.

In Fig. 10(b) the introduction of a static field $\mathbf{h_S} = \mathbf{h}_{\rm ext}$, with $h_{ext,i=\{x,y,z\}} = h_{\rm ext}$, pointing along a different direction from the quenching field $\mathbf{B_Q} = (0, 0, 1)$, breaks the translational symmetry observed before. Indeed, the spin dynamics after the quench and upon an applied field shows a periodic behavior. In particular the dynamics is characterized by two timescales. First, at the femtosecond scale the antiferromagnetic interaction brings the system toward its energy minimum: the spins after the ferromagnetic quench follow the same relaxation as in the absence of applied field at first and form an AF state. Second, at a larger timescale the AF state symmetry is maintained, and the spins precess around the $\mathbf{h}_{\rm ext}$ direction. In particular, as shown in Fig. 5(a) of the main text, the spin trajectories of the A and B sublattices are locked in one limiting circle (red, aligned with the field) or the other (blue, antialigned with the field), giving rise to a $\mathbb{Z}_2$ symmetry of the trajectories. Since the flipping between them is prevented by the interplay of out-of-equilibrium conditions and the uncompensated spins, we conclude that the $\mathbb{Z}_2$ topology of the trajectories is protected. As shown in Fig. 10(b), this nontrivial dynamics which brings the system towards the alignment along the direction of the external field is characterized by an observable timescale. Thus, while for the bcc the staggered magnetic vector stabilizes along the direction of the field at $t = 0.5$ ps [main text, Fig. 5(a)], in the sc cluster the dynamics is characterized by long-lived oscillations, and the alignment is recovered at $t = 20$ ps for $T = 0.001[J_0]$, $h_{\rm ext} = 0.1$. The arising of this intermediate phase between the AF stabilization and the alignment with the external field, characterized by a periodic response of the system to a static field, is exclusively triggered by the uncompensated spins in the AF nanocluster. The duration of the precession phase is increased decreasing the dissipation term γ (Fig. 11a) or the temperature (Fig. 11b).

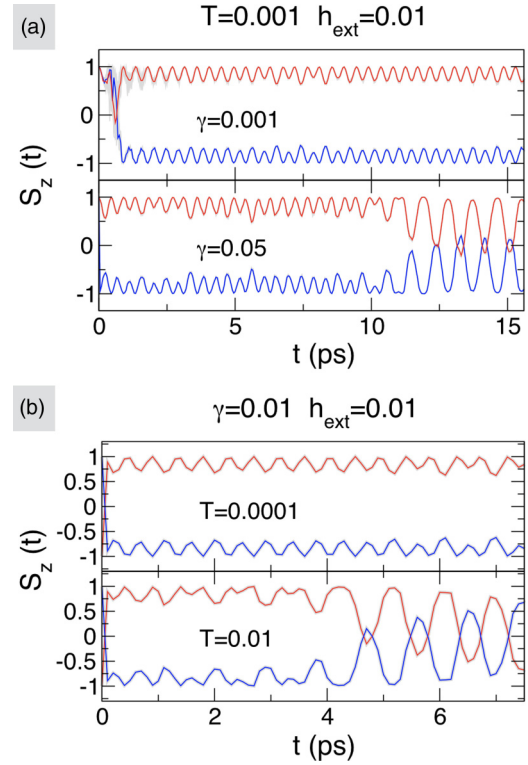

FIG. 11. Time evolution $S_z(t)$ in the sc cluster subjected to a ferromagnetic quench at $t = 0$ and an AC field $\mathbf{h_{AC}} = \mathbf{h}_{\rm ext}\cos(2\pi\omega t)$ for $t > 0$. Blue and red solid lines refer to two sites with opposite magnetic moments after the transient. Results are shown for different values of the dissipation parameter and temperature.

[1] M. Srednicki, Chaos and quantum thermalization, Phys. Rev. E **50**, 888 (1994).

[2] M. Rigol, V. Dunjko, and M. Olshanii, Thermalization and its mechanism for generic isolated quantum systems, Nature (London) **452**, 854 (2008).

[3] J. P. Garrahan, Aspects of non-equilibrium in classical and quantum systems: Slow relaxation and glasses, dynamical large deviations, quantum non-ergodicity, and open quantum dynamics, Phys. A (Amsterdam, Neth.) **504**, 130 (2018).

[4] A. C. Potter, T. Morimoto, and A. Vishwanath, Classification of Interacting Topological Floquet Phases in One Dimension, Phys. Rev. X **6**, 041001 (2016).

[5] M. A. Sentef, M. Claassen, A. F. Kemper, B. Moritz, T. Oka, J. K. Freericks, and T. P. Devereaux, Theory of Floquet band formation and local pseudospin textures in pump-probe photoemission of graphene, Nat. Commun. **6**, 7047 (2015).

[6] F. Wilczek, Quantum Time Crystals, Phys. Rev. Lett. **109**, 160401 (2012).

[7] A. Shapere and F. Wilczek, Classical Time Crystals, Phys. Rev. Lett. **109**, 160402 (2012).

[8] H. Watanabe and M. Oshikawa, Absence of Quantum Time Crystals, Phys. Rev. Lett. **114**, 251603 (2015).

[9] P. Bruno, Impossibility of Spontaneously Rotating Time Crystals: A No-Go Theorem, Phys. Rev. Lett. **111**, 070402 (2013).

[10] J. Zhang, P. W. Hess, A. Kyprianidis, P. Becker, A. Lee, J. Smith, G. Pagano, I. D. Potirniche, A. C. Potter, A. Vishwanath, N. Y. Yao, and C. Monroe, Observation of a discrete time crystal, Nature (London) **543**, 217 (2017).

[11] K. Sacha and J. Zakrzewski, Time crystals: A review, Rep. Prog. Phys. **81**, 016401 (2018).

[12] H. Aoki, N. Tsuji, M. Eckstein, M. Kollar, T. Oka, and P. Werner, Nonequilibrium dynamical mean-field theory and its applications, Rev. Mod. Phys. **86**, 779 (2014).

[13] J. H. Mentink, K. Balzer, and M. Eckstein, Ultrafast and reversible control of the exchange interaction in Mott insulators, Nat. Commun. **6**, 6708 (2015).

[14] R. V. Mikhaylovskiy, E. Hendry, A. Secchi, J. H. Mentink, M. Eckstein, A. Wu, R. V. Pisarev, V. V. Kruglyak, M. I. Katsnelson, T. Rasing, and A. V. Kimel, Ultrafast optical

modification of exchange interactions in iron oxides, Nat. Commun. **6**, 8190 (2015).

[15] M. Schüler, J. Berakdar, and Y. Pavlyukh, Time-dependent many-body treatment of electron-boson dynamics: Application to plasmon-accompanied photoemission, Phys. Rev. B **93**, 054303 (2016).

[16] N. Säkkinen, Y. Peng, H. Appel, and R. van Leeuwen, Many-body Green's function theory for electron-phonon interactions: The Kadanoff-Baym approach to spectral properties of the holstein dimer, J. Chem. Phys. **143**, 234102 (2015).

[17] S. Yan, L. Malavolti, J. A. J. Burgess, A. Droghetti, A. Rubio, and S. Loth, Nonlocally sensing the magnetic states of nanoscale antiferromagnets with an atomic spin sensor, Sci. Adv. **3**, e1603137 (2017).

[18] S. Loth, S. Baumann, C. P. Lutz, D. M. Eigler, and A. J. Heinrich, Bistability in atomic-scale antiferromagnets, Science **335**, 196 (2012).

[19] J.-Y. Bigot, M. Vomir, and E. Beaurepaire, Coherent ultrafast magnetism induced by femtosecond laser pulses, Nat. Phys. **5**, 515 (2009).

[20] D. Dutta, M. Becherer, D. Bellaire, F. Dietrich, M. Gerhards, G. Lefkidis, and W. Hübner, Characterization of the isolated $[Co_3Ni(EtOH)]^+$ cluster by Ir spectroscopy and spin-dynamics calculations, Phys. Rev. B **97**, 224404 (2018).

[21] V. Baltz, A. Manchon, M. Tsoi, T. Moriyama, T. Ono, and Y. Tserkovnyak, Antiferromagnetic spintronics, Rev. Mod. Phys. **90**, 015005 (2018).

[22] M. Vasilakaki, K. N. Trohidou, and J. Nogués, Enhanced magnetic properties in antiferromagnetic-core/ferrimagnetic-shell nanoparticles, Sci. Rep. **5**, 9609 (2015).

[23] K. Chen, A. M. Ferrenberg, and D. P. Landau, Static critical behavior of three-dimensional classical Heisenberg models: A high-resolution Monte Carlo study, Phys. Rev. B **48**, 3249 (1993).

[24] C. Holm and W. Janke, Critical exponents of the classical three-dimensional Heisenberg model: A single-cluster Monte Carlo study, Phys. Rev. B **48**, 936 (1993).

[25] P.-W. Ma, S. L. Dudarev, and J. S. Wróbel, Dynamic simulation of structural phase transitions in magnetic iron, Phys. Rev. B **96**, 094418 (2017).

[26] J. Tranchida, S. Plimpton, P. Thibaudeau, and A. Thompson, Massively parallel symplectic algorithm for coupled magnetic spin dynamics and molecular dynamics, J. Comput. Phys. **372**, 406 (2018).

[27] W. F. Brown, Thermal fluctuations of a single-domain particle, Phys. Rev. **130**, 1677 (1963).

[28] C. Weber, F. Becca, and F. Mila, Finite-temperature properties of frustrated classical spins coupled to the lattice, Phys. Rev. B **72**, 024449 (2005).

[29] J. A. Olive, A. P. Young, and D. Sherrington, Computer simulation of the three-dimensional short-range Heisenberg spin glass, Phys. Rev. B **34**, 6341 (1986).

[30] Y. Miyatake, M. Yamamoto, J. J. Kim, M. Toyonaga, and O. Nagai, On the implementation of the 'heat bath' algorithms for Monte Carlo simulations of classical Heisenberg spin systems, J. Phys. C **19**, 2539 (1986).

[31] C. Weber, L. Capriotti, G. Misguich, F. Becca, M. Elhajal, and F. Mila, Ising Transition Driven by Frustration in a 2D Classical Model with Continuous Symmetry, Phys. Rev. Lett. **91**, 177202 (2003).

[32] F. El-Mellouhi, E. N. Brothers, M. J. Lucero, I. W. Bulik, and G. E. Scuseria, Structural phase transitions of the metal oxide perovskites $SrTiO_3$, $LaAlO_3$, and $LaTiO_3$ studied with a screened hybrid functional, Phys. Rev. B **87**, 035107 (2013).

[33] B. Luan, T. Huynh, and R. Zhou, Simplified TiO_2 force fields for studies of its interaction with biomolecules, J. Chem. Phys. **142**, 234102 (2015).

[34] Y. Weng and S. Dong, Magnetism and electronic structure of (001)- and (111)-oriented $LaTiO_3$ bilayers sandwiched in $LaScO_3$ barriers, J. Appl. Phys. **117**, 17C716 (2015).

[35] T. M. Briere, M. H. F. Sluiter, V. Kumar, and Y. Kawazoe, Atomic structures and magnetic behavior of Mn clusters, Phys. Rev. B **66**, 064412 (2002).

[36] F. Duarte, P. Bauer, A. Barrozo, B. A. Amrein, M. Purg, J. Aqvist, and S. C. L. Kamerlin, Force field independent metal parameters using a nonbonded dummy model, J. Phys. Chem. B **118**, 4351 (2014).

[37] R. Cardias, A. Szilva, A. Bergman, I. D. Marco, M. I. Katsnelson, A. I. Lichtenstein, L. Nordström, A. B. Klautau, O. Eriksson, and Y. O. Kvashnin, The Bethe-Slater curve revisited; new insights from electronic structure theory, Sci. Rep. **7**, 4058 (2017).

[38] L. A. García-Cerda, K. M. Bernal-Ramos, S. M. Montemayor, M. A. Quevedo-Lopez, R. Betancourt-Galindo, and D. Bueno-Baques, Preparation of hcp and fcc Ni and Ni/NiO nanoparticles using a citric acid assisted Pechini-type method, J. Nanomater. **2011**, 162495 (2011).

[39] V. P. Filippova, S. A. Kunavin, and M. S. Pugachev, Calculation of the parameters of the Lennard-Jones potential for pairs of identical atoms based on the properties of solid substances, Inorg. Mater.: Appl. Res. **6**, 1 (2015).

[40] S. Chandrasekhar, Stochastic problems in physics and astronomy, Rev. Mod. Phys. **15**, 1 (1943).

[41] R. Kubo, The fluctuation-dissipation theorem, Rep. Prog. Phys. **29**, 255 (1966).

[42] P.-W. Ma, S. L. Dudarev, A. A. Semenov, and C. H. Woo, Temperature for a dynamic spin ensemble, Phys. Rev. E **82**, 031111 (2010).

[43] P.-W. Ma and S. L. Dudarev, Langevin spin dynamics, Phys. Rev. B **83**, 134418 (2011).

[44] M. J. Han, T. Ozaki, and J. Yu, Electronic structure and magnetic properties of small manganese oxide clusters, J. Chem. Phys. **123**, 034306 (2005).

[45] C. H. Wang, S. N. Baker, M. D. Lumsden, S. E. Nagler, W. T. Heller, G. A. Baker, P. D. Deen, L. M. D. Cranswick, Y. Su, and A. D. Christianson, Antiferromagnetic order in MnO spherical nanoparticles, Phys. Rev. B **83**, 214418 (2011).

[46] J. C. Oberg, M. R. Calvo, F. Delgado, M. Moro-Lagares, D. Serrate, D. Jacob, J. Fernández-Rossier, and C. F. Hirjibehedin, Control of single-spin magnetic anisotropy by exchange coupling, Nat. Nanotechnol. **9**, 64 (2013).